Original Research Paper

Non-Hodgkin Lymphoma Risk Grading Through the Pathological Data by Using the Optimized Convolutional Lymphnet Model

[1]Sivaranjini Nagarajan and [2]Gomathi Muthuswamy

[1]*Department of Computer Science, Auxilium College (Autonomous), Vellore, Tamil Nadu, India*
[2]*Department of Computer Science, Government Arts and Science College, Komarapalayam, Tamil Nadu, India*

Abstract: Diagnosing Non-Hodgkin Lymphoma (NHL) is difficult and often requires specialised training and expertise as well as extensive morphological investigation and, in certain cases, costly immunohistological and genetic techniques. Computational approaches enabling morphological-based decision making are necessary for bridging the existing gaps. Histopathological images can be accurately classified using deep learning approaches, however data on NHL subtyping is limited. However, there is a lack of data about the categorization of lymph nodes affected by Non-Hodgkin Lymphoma. Here in this study, initially image preprocessing was done using the maximal Kalman filter which helps in removing the noise, data augmentation was done to improve the dataset, then the lymph nodal area was segmented using the sequential fuzzy YOLACT algorithm. Finally we trained and optimized an Convolutional Lymphnet model to classify and grade tumor level from tumor-free reference lymph nodes using the grey wolf optimized model by selecting the fitness parameters and optimize it for identifying the patient risk score. The overall experimentation was carried out under python framework. The findings demonstrate that the recommended strategy works better than the state-of-the-art techniques by having excellent detection and risk score prediction accuracy.

Keywords: Non-Hodgkin Lymphoma, Maximal Kalman Filter, Data Augmentation, Sequential Fuzzy YOLACT, Optimized Convolutional Lymphnet Model

Introduction

Lymphocytes cause lymphatic system cancer...lymphoma. This hematologic malignancy ranks third among paediatric malignancies (Ruschenburg *et al*., 1999). Lymphoma is divided into Hodgkin and non-Hodgkin types. In the US, 10% of newly diagnosed lymphomas are Reed-Sternberg cell-positive Hodgkin's Lymphoma (HL) (Orlov *et al*., 2010). Early adulthood and 55+ years are when Hodgkin's lymphoma is most common (Zorman *et al*., 2011). The 2020 global cancer study found 0.4% of new cases and 0.2% of new fatalities were Hepatocellular Carcinoma (HC) (Yan *et al*., 2015). NHL is diagnosed more commonly than HL. This malignancy caused 2.8% of new cancer occurrences and 2.6% of new cancer deaths globally in 2020 (Yan *et al*., 2015).

Lymphoma, like solid tumours, is phased to help assess prognosis and therapy. The Ann Arbour stage method is popular. at 1971, the Committee on Hodgkin's Disease Staging Classification at Ann Arbour, Michigan, devised the Ann Arbour method to classify Hodgkin lymphoma. Non-Hodgkin lymphoma was included to the research (Lisson *et al*., 2022; Brancati *et al*., 2019). According to nodal involvement, the Ann Arbour classification method divides lymphoma patients into four stages I-IV. Based on localised extra lymphatic movement in extra nodal areas, spleen involvement and B symptoms like fever, night sweats and weight loss, the primary stages can be divided into 24 substages.

Staging matters in lymphoma therapy. Hodgkin's disease treatment varies with stage, including different drugs, dosages and rounds of chemotherapy, occasionally with radiation (Tambe *et al*., 2019). Non-Hodgkin lymphoma is treated with chemotherapy and targeted therapy. Stage of sickness and risk variables determine therapy (El Achi *et al*., 2019). Research is underway on

stem cell transplantation and immunotherapy, among other innovative treatments. The disease's course must be accurately categorised to execute different therapy methods (Somaratne *et al*., 2019; Wen *et al*., 2020).

Age, sex, lymphoma type (Hodgkin or Non-Hodgkin), location (nodal or extra nodal) and others are prognostic (Brancati *et al*., 2019). These factors give considerable prognostic information, but the Ann Arbour approach cannot utilise them. Cox regression and survival trees have been used to develop statistical models to add to the Ann Arbour system. However, the current models were not designed for cancer staging, hence they cannot fulfil staging standards. Practical implementations sometimes fail to meet the Cox models' proportionate risks assumption. As opposed to staging systems like the Ann Arbour technique, Cox models do not automatically classify patients into risk groups. Cutoffs and quantiles have divided patients in previous research. There are no defined criteria for classifying patients and the number of groupings is restricted to low-, intermediate and high-risk categories. Survival trees do not create enough groups. Previous study has demonstrated that tree models are inaccurate. So, Cox and survival tree models are not suitable for lymphoma staging for risk score prediction (Krizhevsky *et al*., 2012; Simonyan and Zisserman, 2014; He *et al*., 2016; Haque and Neubert, 2020; Tosta *et al*., 2017).

In recent times, significant progress has been seen in the domain of machine learning and deep learning algorithms, which have shown their efficacy in several solid tumor classifications. This article introduces an optimized model of the Convolutional Lymph net, which serves as a predictive tool for predicting outcomes in patients with Non-Hodgkin Lymphoma.

The work's contributions to its goals are as follows:

1. Maximal Kalman filter normalization was recommended for processing the raw data
2. The lymph node segmentation was done using the sequential fuzzy YOLACT. Here in which the fuzzy rules are incorporated in the YOLACAT mechanism
3. The optimized convolutional lymph net model, which uses GW optimization as its basis, is used to address the NHL risk score prediction issue. The proposed solution exhibits a high degree of adaptability and enhanced reliability

Since the invention of digital computers, several academic disciplines have been able to rapidly advance their use of sophisticated computational tools. Combining spectral analysis with the weighted neighbour distance method. The model's 99% accuracy was obtained using just 30 images of lymphoma. The results of recent studies employing deep learning have been promising. Brancati *et al*. (2019) used the ResNet27

model to categorise three forms of Non-Hodgkin lymphoma (NH). A 27-layer residual convolutional neural network was used to perform the study.

Publicly accessible datasets of digital histology images were used for the performance assessment and the findings from many deep neural networks, including UNet and ResNet, were compared and contrasted. The results of the experiments show an improvement of 5.06% in the F-score for the detection job and an improvement of 1.09% in the accuracy measure for the classification test. A fully automated system based on Deep Neural Networks was first shown by Tambe *et al*. (2019) The lymphoma diagnosis model developed by El Achi *et al*. (2019) is based on a Convolutional Neural Network (CNN) algorithm trained using Deep Learning methods. Diffuse large B-cell lymphoma, Burkitt lymphoma, small lymphocytic lymphoma and benign instances were all included during the development of the model. Using a test set of 240 images, it was determined that the diagnostic accuracy of the test results was excellent, reaching 95%, (Somaratne *et al*., 2019) presented a deep learning framework that makes use of transfer learning and fine-tuning approaches. When compared to the model's initial predictions for the same set of testing photos, the proposed technique shows a considerable improvement in prediction accuracy, improving it from an initial value of 12-52%. They used transfer learning with the RestNet50 pretrained model to diagnose seven subtypes of lymphoma with 91.6% (Wen *et al*., 2020) accuracy, which is higher than previous research. The kinds were chosen because of the difficulties in detecting them and the fact that they proceed asymptomatically. More work is needed to help in the diagnosis of lymphomas such composite follicular and mantle cell, which are rare and poorly understood yet may save many lives.

Problem Statement

In accordance with prior research efforts, we used deep learning techniques coupled with optimization methods to effectively categorize lymphoma subtypes for the purpose of diagnosis, yielding a commendable accuracy rate of 99.6%. The selection of types was based on their characteristic of asymptomatic growth and the challenges associated with their identification. In some situations, the diagnosis and categorization of lymphomas might present significant complexity owing to uncertainties surrounding the assessment of morphological and immune-phenotypical characteristics, as well as the biological continuum. Since many lymphomas, including composite follicular, NHL and mantle cell, are not well-defined, there is a pressing need for more research into their identification and diagnosis in order to save the lives of many people.

Materials

Data from the Medical University of Gdask was used to compile the Lymphoma Image Dataset (LID), which was then archived in the ZMDL-GUMED. The dataset comprises of 323 pictures of 224-by-224-pixel, which is the This dataset is available at https://mostwiedzy.pl/en/open-research-data/diffuse-non-hodgkin's-lymphoma-male-60-tissue-image-2210630020351581,2210630020351581-4.

This tissue sample was collected from Medical University Gdask and is housed at ZMDL-GUMED; the picture is a histological examination of the hematopoietic and reticuloendothelial SYSTEMS. Panoramic 250 3DHistech slide scanner (20x magnification) used to capture example picture, which was then converted to DICOM format.

Here's the rundown on the patient, the sample and the diagnosis:

Patient

- Age: 60
- Clinical description: Splenomegaly
- Gender: Male

Diagnosis

- Classification: ICD-10_10-20
- Classification code: Chapter II - Neoplasms
- Diagnosis: Diffuse non-Hodgkin's lymphoma

Result of the histopathological examination: High grade B cell lymphoma. Tumor immunophenotype: CD20(+), CD3(-), CD79(+), bcl2(30%+), bcl6(40%+), cmyc(30%+), MUM1(focallt+), CD10(focally+), CD5(-), CD23(-), ALK1(-), CD30(-), CD15(-), CD138(-), EBER(-), CK AE1/3(-). Ki67- 90%.

Sample

- Material: FFPE
- Collecting method: Surgical specimen
- Topography: Hematopoietic and reticuloendothelial systems
- Organ: Hematopoietic and reticuloendothelial systems
- Tissue: Spleen
- Type of staining: Positive/IHC
- Staining: Not applicable
- Antibody: CD 30

Methods

The schematic representation of the suggested methodology was illustrated in Fig. 1. Figure 1 depicts the suggested diagnostic system for this investigation.
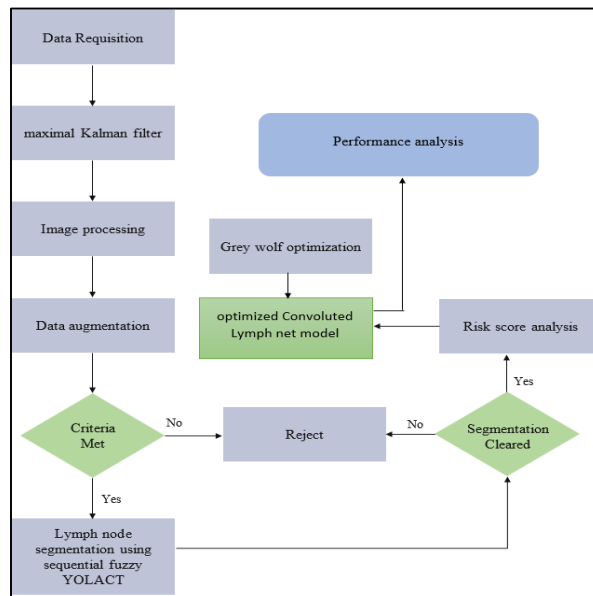

Fig. 1: Schematic representation of the suggested methodology

Technology

- Equipment: Panoramic 250 3DHistech
- Lens: 20x

Organization

- Source: Medical University Gdańsk"

Pre-processing

Maximal Kalman filter may help reduce the noise which has a major impact on image quality because of inaccuracy and error pattern. Therefore, a noisy picture model is provided by, to characterise the noise-reduction effect:

$$P_S(b, a) = I_S(b, a) - I_P(b, a) \; b \in [1, B] \; a \in [1, A] \qquad (1)$$

Ideal two-dimensional image without any interference is denoted by the notation $I_p(b, a)$. On the other hand, the picture that has been corrupted by mistakes is represented by $I_s(rb, a)$. Last but not least, $P_S(b, a)$ indicates how mistake correction affected the original picture. A and B are two independent variables that measure the same thing: The number of range sampling points and the number of pixel frames. The "r" and "a" variables denote the range and error points, respectively and their respective pixel coordinates. Considering $I_p(b, a)$, $I_s(b, a)$ and $P_S(b, a)$ as two-dimensional matrices is possible.

The error range is often corrected when the photograph is being focused, thus there is usually very little variation. This study assumes that the severity of the mistake is constant in the range direction to keep things

nice and simple while yet being as generic as possible. Accordingly, Eq. (1) may be recast for any particular frame as:

$$I_S(b) = I_P(b) + P_S \; b \in [1, B] \tag{2}$$

There is an erroneous part of $I_p(b)$ that persists while P_s is present. $I_p(b)$ represents the noise is introduced into the equation, the estimation of intensity is transformed into the estimation of the direct current component. As a result, a unique method is proposed for calculating noise error by using the maximum Kalman filtering method. I_s for a linear system, the desired state value is represented by the symbol P_S, which stands for the system's output.

The stochastic difference equation shown below is often used to estimate the error value in the context of a discrete process:

$$x_l = Ax_{l-1} + \omega_{l-1} \tag{3}$$

In this equation, x represents the linear state of P_s, A is the linear data transition matrix and is the processed noise. Observation equation is then defined as:

$$z_l = Hx_l + v_l \tag{4}$$

Given these parameters, we may define z as the observed P_s, state, H as the observation gain matrix and v as the observation noise.

It is often considered that they are unrelated to one another and have a white Gaussian distribution:

$$p(\omega) \sim N(0, Q), p(v) \sim N(0, \Re) \tag{5}$$

where, Q in the probability density function stands for the variance $p(.)$ of the system, whereas R stands for the variance of the observations.

Taking into account the data in (2), the amount that needs approximation is P_s. Parameter A in Eq. (3) is set to 1 since Os is a constant and stays in the same place at all times. Equation (4), the observation noise is denoted by the variable $I_0(b)$, $b \in [1, B]$ where, b is in the range $[1, B]$. This estimate uses the pixel value of the distorted image as the measurement value of the system, yielding no further information. This means that in Eq. (4), H must have a value of 1. The covariance of the system may be expressed both as a prior estimate and a posterior estimate using the above model:

$$\begin{aligned} P_l^- &= E[(x_l - \dot{x}_l^-)(x_l - \dot{x}_l^-)^T] \\ P_l &= E[(x_l - \dot{x}_l)(x_l - \dot{x}_l)^T] \end{aligned} \tag{6}$$

where, $\dot{x}_l^-$ and $\dot{x}_l$ are the kth represents the difference between the original and most recent predictions of the system's condition is referred to as the "posterior estimate."

Following is a derivation of both the time update equations and the state update equations for the maximum Kalman filter. Update equation:

$$\begin{aligned} K_l &= \frac{P_l^-}{P_l^- + \Re}, \dot{x}_l = \dot{x}_l^- + K_l(z_l - \dot{x}_l^-) \\ P_k &= (I - K_l)P_l^- \end{aligned} \tag{7}$$

Statistical model:

$$\dot{l}_l^- = \dot{x}_{l-1}, P_l^- = P_{l-1} + Q \tag{8}$$

where, K_l is the unity matrix (I) plays a role in determining the blending factor that minimises the covariance of a posteriori error, which is in turn determined by the covariances of the process noise (Q) and the observation noise (R).

When used iteratively, the maximum Kalman filter proves to be an accurate tool for estimating the magnitude of error across all columns. The estimated error in each column may then be subtracted to achieve error suppression.

Augmentation

When augmenting image data with varying height and width dimensions, the technique of cropping may be used as a beneficial step, whereby a significant portion of each picture is removed. In this demonstration, we will illustrate a method for doing random cropping of images. The selection of cropped coordinates (H_k, z_k) is influenced by the original dimensions of the picture and these coordinates are selected based on the placement of the border (x, i):

$$\begin{aligned} H &= round(H'I_H), \quad I = round(H'I_z), \\ H' &\sim Beta(\beta, \beta), \quad I' \sim Beta(\beta, \beta) \end{aligned} \tag{9}$$

where, $\beta \in (0, \infty)$ represents the parameter which is a variable in a mathematical or statistical model. The function round ($\cdot$) denotes the rounding method. The mechanical determination of cropping dimensions occurs subsequent to the identification of the boundary location (w, h) is known. (X_L, I_L) of the images k, i.e., $X_1 = X_3 = X$, $X_2 = X_4 = I_x - X$, $h_1 = h_2 = h$ and $I_3 = I = I_H - h$. alternatively, sizing the crop tool to fit the images (w_k, h_k), We choose the order by chance. (Y_k, Z_k) shows the cutoff edges as:

$$\begin{aligned} H_l &\sim \mathcal{U}(0, I_H - X_l), \\ Z_l &\sim \mathcal{U}(0, I_z - I_l) \end{aligned} \tag{10}$$

Then the images can be cropped.

Segmentation

By splitting the process of segmentation of instances into two smaller subtasks that are done in parallel, You

Only Look At CoefficienTs (YOLACT) is able to address the lymph node regions. A linear fuzzy combination, is performed using the prototype masks and mask coefficients generated by the parallel branches.

Step 1: Rule Establishment

To establish its rules, YOLACT use a Fuzzy mechanism:

$$\text{Rule 1:} \, If \, U_1 \, is \, B_j \, and \, U_2 \, is \, Z_j, \, then$$

$$\text{Rules}_j = sU_j + t_jU_{j+1} + u_j$$

$$\text{Rule 2:} \, If \, U_1 \, is \, B_{j+1} \, and \, U_2 \, is \, Z_{j+1}, \, then$$
$$\text{Rules}_{j+1} = s_{j+1}U_j + t_{j+1}U_{j+1} + u_{j+1}$$

where, the sets B_i, Z_i, B_{i+1} and Z_{i+1} are all fuzzy ones. The many feature values collected so far are denoted by U_i and U_{i+1}. Training is expected to cause changes to the parameters s_i, t_i, u_i, s_{i+1}, t_{i+1} and u_{i+1}. The necessary parameters are fine-tuned using the interference technique for improved results.

Step 2: Lymph Node Based Feature Extraction

To get the fuzzy entropy property, the following formula is utilized:

$$f = \sum_{ij=0}^{N-1} Q_{ij}(-\ln Q_{ij}) \tag{11}$$

Mean, Variance, Skewness, Kurtosis and Moment are the five texture characteristics that may be calculated from the determined gradient matrices. Gradient features are produced when the his of a gradient matrix has been created. For gradient values in the range (-255, 255), this histogram is computed. Here is how the gradient (Kurtosis) characteristic looks like:

$$f = \sum_{sv} \frac{\text{His} \, (v+255)(v-\mu)^4}{\text{Total number of pixels}} \tag{12}$$

Step 3: ROI Extraction

The S_v is expected to go the direction with the smallest f-value, ROI. To restate: The fuzzy rule for s-associations is:

$$D(N_\beta, S_v) = \begin{cases} 1, if \, Q(N_\beta, S_v) = min\{Q(N_\beta, S_v) \neq 0\} \\ 0, otherwise \end{cases} \tag{13}$$

The *IoU* is defined as the fraction of a region that is shared by the ground-truth and the forecasted regions. The Intersection over Union metric quantifies the degree of similarity between the obtained segmentation outcomes and the reference ground truth. The Intersection over Union (IoU) is a scalar ranging between 0 and 1, where a higher value signifies a higher level of accuracy in segmentation. The Intersection over Union metric was determined in the following manner:

$$IoU = \frac{TP}{TP+FP+FN} \tag{14}$$

To combine the *ROI* estimates, a sigmoid-shaped nonlinear combination is required:

$$M = \sigma(QC^U) \tag{15}$$

Here, *M* is the segmentation result of the segmentation method, *Q* is the ground truth and *P C* is the number of pixels in the corresponding set.

Here, *u* represents the number of predicted *ROI* regions after undergoing non-maximum suppression. Upon completion of the aforementioned processes, the network generates the ultimate segmentation outcome.

NHL Prediction

The purpose of this research is to optimise a complex lymph net using the grey wolf algorithm for *NHL* prediction. Following is a definition of the objective function:

$$acc = CLN(\vec{Ip}, \vec{U}, Td_i) \tag{16}$$
$$\underset{\vec{Hp} \in \mathbb{R}^k}{maximize} acc \, CLN(\vec{Ip}, \vec{U}, Td_i) \, where < i_{\max}$$

Inputs are represented by $\vec{Ip}, \vec{U}, Td_i . \vec{Hp}$ and the resulting mathematical equation illustrates the functional connection of the *LN* architecture. The k-dimensional hyperparameter vector is represented by $\vec{Hp}$. The weight of a Connected-Loop Network (*CLN*) is denoted by the vector $\vec{U}$. Td_i is an arbitrary selection from the whole set of training data. The above function is intended to provide a measure of the model's precision. The purpose of the function represented by Eq. (16) is to optimise the CLN's hyper-parameters in order to achieve the highest possible accuracy. The number of times CLN tries to get the hyper-parameters just right may be controlled by the user using the $i_{\max}$ option. The time needed to optimise increases when $i_{\max}$ rises over a certain threshold. To make the model as cost-effective as possible, the user must intentionally choose the value of $i_{\max}$.

After the CLN architecture has been established, four separate steps parameter encoding, population initialization, fitness evaluation and next-generation population construction are taken to optimise the network's hyper-parameters using GWO. In the context of the GWO approach, communication is established between the exploitation and exploration processes. This communication occurs within two distinct groups of grey wolves, each operating independently. The grouping hunt strategy is employed, utilising four specific types of grey wolves that have been designed for efficient utilisation in the optimisation process. In contrast, the exploratory approach characterised by chaotic grouping involves deploying several scouts to conduct examinations in a comprehensive way.

The GWO algorithm is provided as shown below:

Algorithm 1: Grey wolf optimization process

*"**Input:** Segmented output*
***Output:** Optimized value*
*Step*1*: The parameters are initialized,*
    $_{UCD}$ signifies the Upper limit lower limit
   Search agents_num τ_{s_ag}) = 30;
     Max_iteration max_{iter} = 100;
Lower band $l_b = min$ (u_{cd});
Upper band $u_b = max$ (u_{cd})
Dimensions $d_b = size$ (u_b, 2)
Step 2: Alpha, beta and delta positions are being initialized
    Alpha_pos $\alpha_{pos} = zeros$ (1, d_b)
    beta_pos $\beta_{pos} = zeros$ (1, d_b)
    delta_pos $\gamma_{pos} = zeros$ (1, $_{db}$)
    position $pos_{data} = rand$ (τ_s_ag), 1) (u_b - l_b) +l_b*
Step 3: objective function is estimated
    while 1< max_{iter}
      for i = 1: size (pos_{data}, 1)
        flag4ub = pos_{data} (I, :) > u_b
        flag4lb = pos_{data} (I, :) <l_b
        *pos_{data} (I, :) = pos_{data} (i, :) * (flag4ub+*
        flag4lb) + u_b flag4ub + l_b* flag4lb*
$d_b = size$ (PI, 2)
   Kp = PI (d_b, pos_{data})
   Ki = size (PI, 2)

$$obj_{fn} = -20 * exp(-2 * \sqrt{\sum PI^2})/2$$
$$-exp(\sum cos(2\pi * PI) /d_b) + 20exp$$

Step 4: alpha, beta and delta positions are updated,
    If $obj_{fun} < \alpha_{pos}$
     $\alpha_{pos} = obj_{fun}$
$\alpha_{pos} = pos_{data}$ (I,:)
End
If $obj_{fun} < \alpha_{pos}$ && $obj_{fun} < \beta_{pos}$
    $\beta_{pos} = obj_{fun}$
End
If $obj_{fun} < \alpha_{pos}$ && $obj_{fun} > \beta_{pos}$ && $obj_{fun} < \gamma_{pos}$
$S_n = obj_{fun}$
End
 end
end"

The Convolutional Neural Network's (Fig. 2(a)) hyperparameters are encoded as a vector of k parameters during the parameter encoding step. The Convolution layer's (CV) Kernel size (Ks), the Number of kernels (Nk), the Pooling layer's (Ps) kernel size and the Dropout rate (Dr) are all examples of hyperparameters. The parameters are randomised within the allowed range. When the ith parameter vector is exactly described as in Eq. (17), we say that it acts as an agent:

$$\overrightarrow{IP}_i = \{Q_{i1}, Q_{i2}, Q_{i3}, ... Q_{ik}\} \tag{17}$$
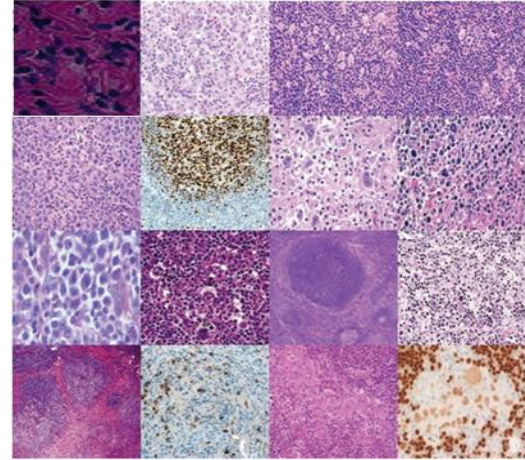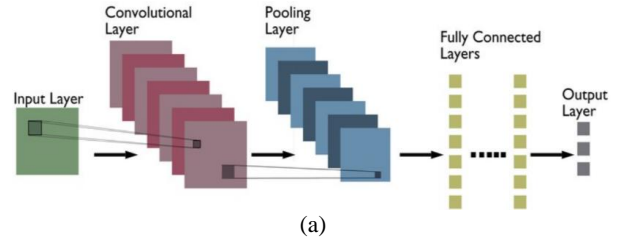

(a)

(b) Sample input

Fig. 2: (a) Suggested network architecture; (b) The sample histopathological input was illustrated

Including three convolution layers, three dropout layers and three pooling layers results in a total of twelve hyper-parameters that make up the parameter vector.

After the CLN hyper-parameters have been encoded, an initial population S_n of n agents will be randomly generated:

$$S_n = \{\overrightarrow{IQ}_1, \overrightarrow{IQ}_2, \overrightarrow{IQ}_3 ... ... \overrightarrow{IQ}_n\} \tag{18}$$

Equations 17-18 are used to generate the Grey Wolf Optimizer (GWO) coefficient vectors $\vec{A}$ and $\vec{C}$. Changing the values of the random parameters A and C allows the candidate solution to display hyperspheres of different radii. According to Eq. (19), when $\vec{X}_\alpha, \vec{X}_\beta, \vec{X}_\partial$ move, the rest of the agents' locations are updated accordingly. After these hyperparameters have been fine-tuned, we can create optimal CLN models. Categorical risk score has the following meaning:

$$RS = -\sum_{i=1}^{N} y_i \cdot log\ \hat{y}_i, RS = -\sum_{i=1}^{N} y_i \cdot log\ \hat{y}_i \tag{19}$$

N here stands for the total number of categories. Model-predicted value for the ith class is denoted by $\hat{y}_i$, whereas y_i stands for the corresponding risk-objective value.

Performance Analysis

The pytorch framework was used to train the experiment in an environment consisting of an Intel (R)

Xeon (R) Gold 5220 CPU and a GeForce RTX 2080 Ti GPU. Python is the language used for programming. This study uses 374 TIF-formatted photos from an open-source experimental data set made available on an official public website. The sample histopathological input was illustrated in Fig. 2(b).

The disease prediction output for the sample images are illustrated from the Fig. 3. As of from the Fig. 4 the images in which ROI are segmented and the diseased lymph nodes are identified and the NHL can be classified precisely by using the suggested classifier.

The score of a risk is determined by the specified values of chance and effect. The integration of probability and effect thresholds culminates in the formation of a risk matrix, which serves as a visual representation of the potential scores that a risk may attain. Depends upon the depressive symptoms severity level was determined and risk level was pointed.

The square of the error is calculated in a manner similar to that of the variance. The MSE is calculated by square rooting the difference between the observed value and the anticipated value. Add up the squares of all the observations and then divide by the total number of observations. Figure 5 shows that, in comparison to predicting illness nodes, the prediction error was lower.

Based on the facts shown in Fig. 6 the disparity between the validation accuracy and the training accuracy may be attributed to the model's prior exposure to the training data, which results in a higher level of familiarity. Conversely, the validation data comprises novel data points that are unknown to the model. The precise determination of perspectives may be accomplished by using the classifier that is suggested, in Fig. 6.

Figure 7, it is possible to visually discriminate between groups consisting of people with and without problems. Multiple metrics, such as accuracy, sensitivity, specificity, precision and the f1 measure, were used to evaluate the classification algorithms. Therefore, the criteria specified by the confusion matrix are used to evaluate the show. With respect to the current situation, when a prediction correctly identifies the existence of liver disease in a patient, this is called a True Positive (TP). A False Positive (FP) is an incorrect diagnosis that wrongly suggests that a patient has liver disease. A True Negative (TN) is a successful prediction result in which a patient is appropriately diagnosed as having no liver disease. To anticipate incorrectly that a patient does not have liver disease is an example of a False Negative (FN). Quantifying the gap between sound-to-patient capacity ratio relies heavily on the accuracy of the prediction model.

Correctly identifying positive, negative, false positive and false negative cases is how classification accuracy is evaluated:

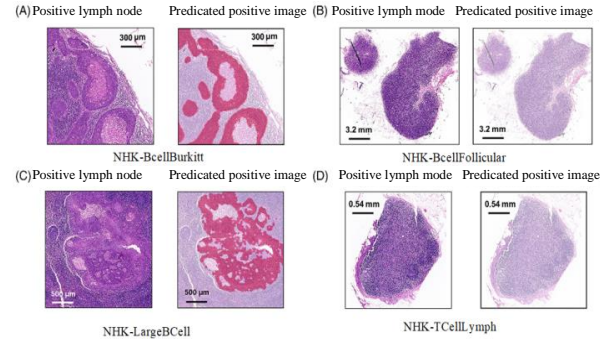$$Accuracy = \frac{(TP + TN)}{(TP + FP + TN + FN)} \qquad (20)$$
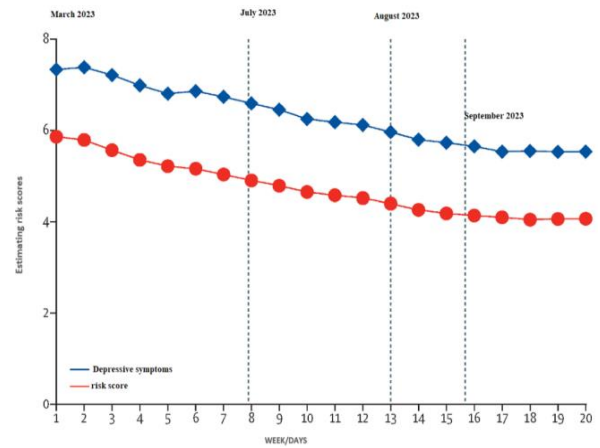

Fig. 3: Simulated output
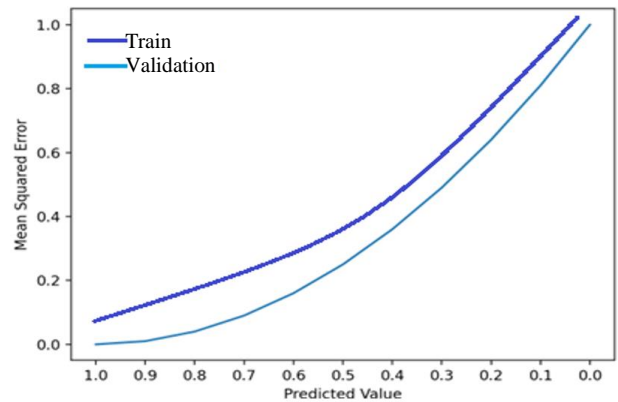

Fig. 4: Risk score

Fig. 5: MSE calculation

The percentage of patients correctly recognized as having liver disease is reported by the sensitivity test. The positive results of the test are highlighted throughout the text. It's also known as the *True Positive Rate* (*TPR*) or *Recall* rate:

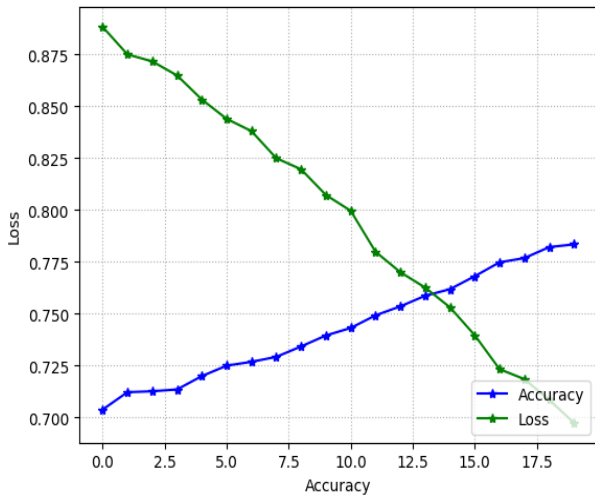$$Recall = \frac{True\ Positive}{(True\ Positive + False\ Negative)} \qquad (21)$$

Fig. 6: Accuracy Vs loss
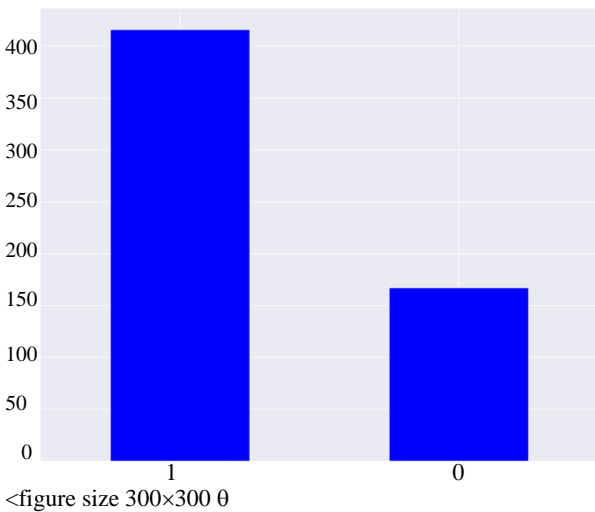

<figure size 300×300 θ

Fig. 7: Target classification

Particularity entails the manifestation of adverse outcomes associated with the condition. It provides an assessment of the prevalence of the condition among the patients. It is often referred to as the True Negative Rate (TNR).

Precision is the rate of success in recognizing real positive situations; it is also known as the positive predictive value. The metric gives a measure of how often classifier algorithms provide accurate predictions of favorable outcomes:

$$Precision = \frac{True\ Positive}{(True\ Positive + False\ Positive)} \tag{22}$$

The $F1$ metric quantifies the precision of a model by considering a combination of accuracy and recall. The metric provides the ratio of both False Positives (FP) and False Negatives (FN) generated by a model:

$$F1 = \frac{2*(Recall * Precisiion)}{(Recall + Precision)} \tag{23}$$

Multiple metrics, such as accuracy, sensitivity, specificity, precision and the $F1$ measure, were used to evaluate the classification algorithms. With respect to the current situation, when a prediction correctly identifies the existence of disease risk score in a patient, this is called a True Positive (TP). A False Positive (FP) is an incorrect diagnosis that wrongly suggests that a patient has high risk score. A True Negative (TN) is a successful prediction result in which a patient is appropriately diagnosed as having no disease with less risk score. To anticipate incorrectly that a patient does not have disease is an example of a False Negative (FN).

Results and Discussion

The results shown in Fig. 8 demonstrate the effectiveness of the proposed technique, as seen by the high levels of accuracy (99.6%), precision (97%), recall (94%) and F-score (92%). These metrics indicate the methodology's efficiency in achieving satisfactory outcomes.

Figure 9 the suggested methodology express satisfied performance. Figure 10 shows the results of an analysis of NHL disease using the proposed categorization system. Here, the effectiveness of the Process will be reflected in a little deviation from both the ground truth and the initial forecast.

The ROC curve in two dimensions is seen in Fig. 11. Positive rates are shown on the x-axis, while the actual rates are shown on the y-axis. The threshold ranges from 0-1 (upper right to lower left). Graphs depict the results of each criterion classification. The classifier's accuracy is 99% if its AUC is 99.9% or higher.

Hence as of from the result obtained from the Table 1 the suggested methodology express satisfied outcomes over NHL risk score prediction when compared to other existing mechanism in use".

Table 1: Summary of existing methodologies about NHL disease prediction (Lisson *et al.*, 2022)

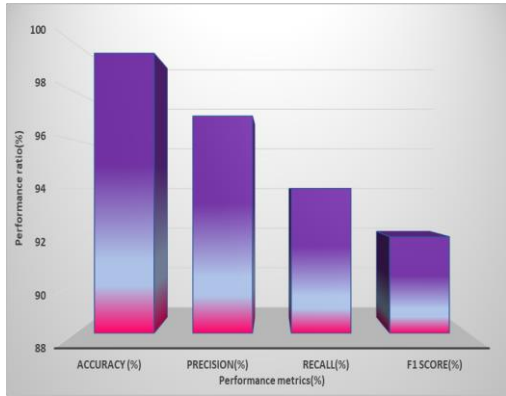| Deep learning models	Accuracy	Precision	Sensitivity/Recall	F1-Score	AUC
Own 3D Net [25]	0.700±0.02	0.710±0.02	0.70±0.020	0.690±0.010	0.70±0.04
3D DenseNet [25]	0.590±0.05	0.640±0.07	0.59±0.050	0.570±0.060	0.58±0.13
SEResNet50 [25]	0.620±0.04	0.650±0.07	0.62±0.050	0.600±0.040	0.62±0.06
Proposed	99.600	97	94	92	99.90

Fig. 8: Performance analysis of the suggested methodology
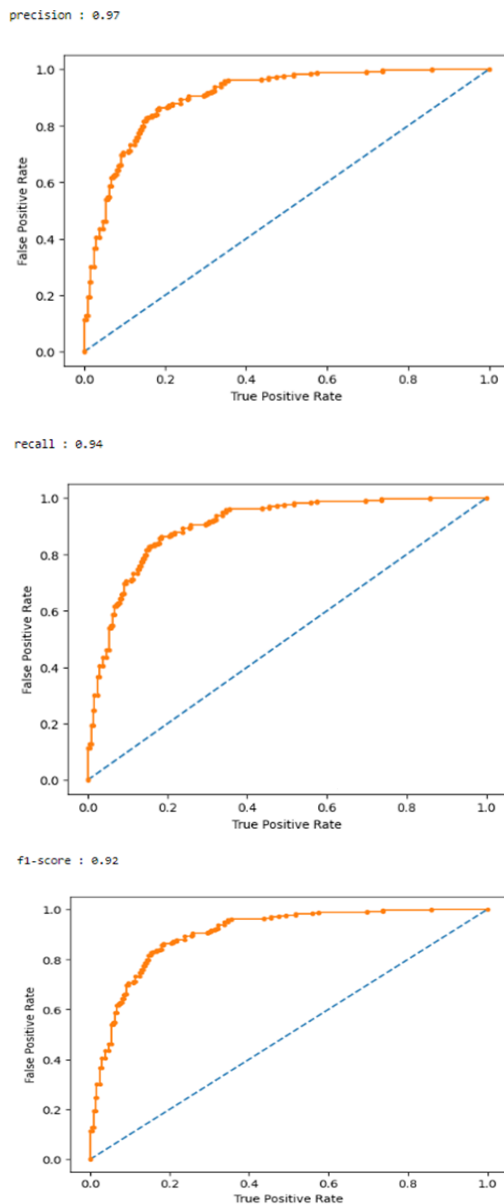

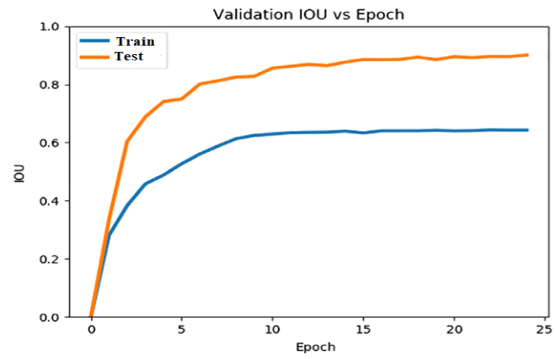**Fig. 9:** Proposed methodology performance ratio analysis
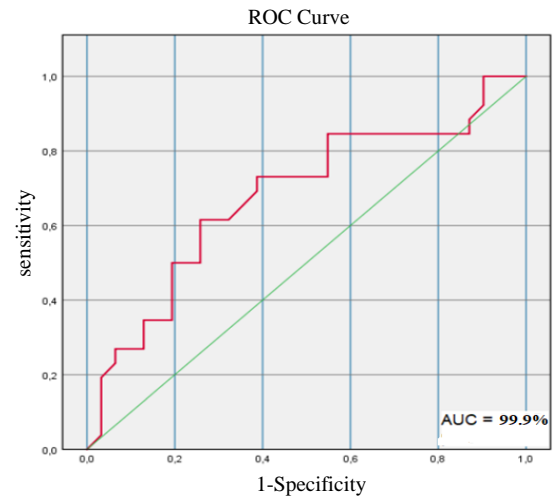

Fig. 10: Epoch Vs. IoU

Fig. 11: ROC evaluation

Conclusion

NHL is a serious health problem and preventing it, treating it early and diagnosing it correctly are all more important than merely trying to discover a cure. According to the review of prior work, various attempts have been made to use deep learning algorithms for NHL risk prediction which helps to give efficient treatment for the patients. Nonetheless, a major obstacle remains the discovery of relevant lymph nodes that may successfully identify and grade disease at an early stage. This research presents a novel and improved model for grading of NHL disease. The proposed model had behaviour similar to a traditional neural network leading to an impressively high accuracy score of 99.6% when classifying illnesses and grading the risk score. Upcoming studies will concentrate on implementing ensemble based methodology to aid in the diagnosis of NHL disease. Efforts will also be made to remove superfluous features from existing feature sets in an attempt to improve the accuracy of detection strategies. Our

model may become more accurate at distinguishing between those with high risk score and those with low risk score. The main limitation of this study is the dataset in which the proper information was not obtained. In future the medications recommendations based on the risk score was highly focused.

Acknowledgment

Funding Information

Author's Contributions

Sivaranjini Nagarajan: Designed, analysis and acquisition of data.

Gomathi Muthuswamy: Reviewed and Organized the study.

Ethics

Ethical issues (including plagiarism, data fabrication, double publication) have been completely observed by the authors.

Conflicts of Interest

The authors declare that they have no competing interests.

References

Brancati, N., De Pietro, G., Frucci, M., & Riccio, D. (2019). A deep learning approach for breast invasive ductal carcinoma detection and lymphoma multi-classification in histological images. *IEEE Access*, *7*, 44709-44720.
https://doi.org/10.1109/ACCESS.2019.2908724

El Achi, H., Belousova, T., Chen, L., Wahed, A., Wang, I., Hu, Z., ... & Nguyen, A. N. (2019). Automated diagnosis of lymphoma with digital pathology images using deep learning. *Annals of Clinical and Laboratory Science*, *49*(2), 153-160.
http://www.annclinlabsci.org/content/49/2/153.short

Haque, I. R. I., & Neubert, J. (2020). Deep learning approaches to biomedical image segmentation. *Informatics in Medicine Unlocked*, *18*, 100297.
https://doi.org/10.1016/j.imu.2020.100297

He, K., Zhang, X., Ren, S., & Sun, J. (2016). Deep residual learning for image recognition. In *Proceedings of the IEEE Conference on Computer Vision and Pattern Recognition* (pp. 770-778).
https://doi.org/10.1109/CVPR.2016.90

Krizhevsky, A., Sutskever, I., & Hinton, G. E. (2012). Imagenet classification with deep convolutional neural networks. *Advances in Neural Information Processing Systems*, *25*.
https://doi.org/10.1145/3065386

Lisson, C. S., Lisson, C. G., Mezger, M. F., Wolf, D., Schmidt, S. A., Thaiss, W. M., ... & Goetz, M. (2022). Deep neural networks and machine learning radiomics modelling for prediction of relapse in mantle cell lymphoma. *Cancers*, *14*(8), 2008.
https://doi.org/10.3390/cancers14082008

Orlov, N. V., Chen, W. W., Eckley, D. M., Macura, T. J., Shamir, L., Jaffe, E. S., & Goldberg, I. G. (2010). Automatic classification of lymphoma images with transform-based global features. *IEEE Transactions on Information Technology in Biomedicine*, *14*(4), 1003-1013.
https://doi.org/10.1109/TITB.2010.2050695

Ruschenburg, I., Kneitz, S., Brinck, U., Korabiowska, M., Harms, H., & Droese, M. (1999). Myoepithelial sialadenitis versus low-grade non-Hodgkin's lymphoma of the salivary gland in FNAB: Is discrimination by means of an image processing system possible?. *In vivo (Athens, Greece)*, *13*(6), 515-518.
https://europepmc.org/article/med/10757047

Simonyan, K., & Zisserman, A. (2014). Very deep convolutional networks for large-scale image recognition. *arXiv preprint arXiv:1409.1556*.
https://doi.org/10.48550/arXiv.1409.1556

Somaratne, U. V., Wong, K. W., Parry, J., Sohel, F., Wang, X., & Laga, H. (2019, December). Improving follicular lymphoma identification using the class of interest for transfer learning. In *2019 Digital Image Computing: Techniques and Applications (DICTA)* (pp. 1-7). IEEE.
https://doi.org/10.1109/DICTA47822.2019.8946075

Tambe, R., Mahajan, S., Shah, U., Agrawal, M., & Garware, B. (2019, January). Towards designing an automated classification of lymphoma subtypes using deep neural networks. In *Proceedings of the ACM India Joint International Conference on Data Science and Management of Data* (pp. 143-149).
https://doi.org/10.1145/3297001.3297019

Tosta, T. A. A., Neves, L. A., & do Nascimento, M. Z. (2017). Segmentation methods of H&E-stained histological images of lymphoma: A review. *Informatics in Medicine Unlocked*, *9*, 35-43.
https://doi.org/10.1016/j.imu.2017.05.009

Wen, K. W., Fakhri, B., Menke, J., Ruiz-Cordero, R., Gill, R. M., & Ohgami, R. S. (2020). Complexities in the diagnosis of large B-cell lymphomas, classic Hodgkin lymphomas and overlapping peripheral T-cell lymphomas simplified: An evidence-based guide. *Annals of Diagnostic Pathology*, *46*, 151534. https://doi.org/10.1016/j.anndiagpath.2020.151534

Yan, T., Liu, Q., Wei, Q., Chen, F., & Deng, T. (2015). Classification of lymphoma cell image based on improved SVM. In *Advances in Applied Biotechnology: Proceedings of the 2ⁿᵈ International Conference on Applied Biotechnology (ICAB 2014)-Volume I* (pp. 199-208). Springer Berlin Heidelberg. https://doi.org/10.1007/978-3-662-45657-6_21

Zorman, M., Sánchez de la Rosa, J. L., & Dinevski, D. (2011). Classification of follicular lymphoma images: A holistic approach with symbol-based machine learning methods. *Wiener Klinische Wochenschrift*, *123*. https://doi.org/10.1007/s00508-011-0091-z